

Development of Galectin-7-Specific Nanobodies: Implications for Immunotherapy and Molecular Imaging in Cancer

Rita Nehmé, Marlène Fortier, Myriam Létourneau, Camille Fuselier, Philippine Granger Joly de Boissel, Alyssa Dumoulin, Brigitte Guérin, Véronique Dumulon-Perreault, Samia Ait-Mohand, Otman Sarrhini, Sacha T. Larda, Yarileny Castellanos Villamizar, Mighel Bernier, Natalia Porębska, Łukasz Opaliński, David Chatenet, Nicolas Doucet, and Yves St-Pierre*



Cite This: *J. Med. Chem.* 2025, 68, 8484–8496



Read Online

ACCESS |



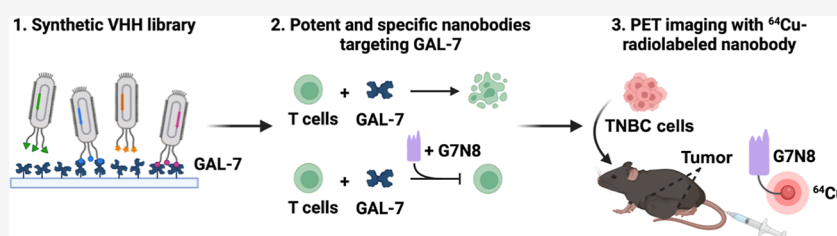
Metrics & More



Article Recommendations



Supporting Information



ABSTRACT: Galectins play significant roles in regulating immune responses, posing challenges for cancer immunotherapy. The development of galectin inhibitors has been limited by their high structural homology and the lack of noninvasive imaging tools to identify potential responsive patients. We developed 12 galectin-7-specific inhibitors using nanobodies (Nbs) and identified G7N8 as the lead Nb. G7N8 was conjugated with the NOTA chelator, labeled with copper-64 ($[^{64}\text{Cu}]\text{Cu}$), and used as a radiotracer for PET imaging in a triple-negative breast cancer (TNBC) mouse model. Nbs demonstrated high affinity for galectin-7, with no binding activity for other galectins tested. The lead Nbs inhibited galectin-7 binding to T-cell glycoreceptors and reduced subsequent apoptosis. PET imaging with $[^{64}\text{Cu}]\text{Cu}$ -NOTA-G7N8 showed selective radiotracer accumulation at 20 h ($P = 0.001$). We developed galectin-7-specific Nbs that inhibit T-cell apoptosis and enable PET imaging of TNBC, providing novel tools for investigating immune regulation and enhancing cancer immunotherapy.

INTRODUCTION

Galectins (GALs) are a family of highly conserved proteins that share a characteristic carbohydrate recognition domain (CRD).¹ They are known for their ability to bind β -galactosides, although their selectivity for glycoconjugates varies depending on the structure and organization of their CRD. Galectins are generally classified into three main types. The first group, prototype GALs, contains a single CRD from approximately 14–20 kDa. These GALs typically form homodimers, enabling them to cross-link glycoproteins and glycolipids on cell surfaces or within extracellular matrices. The second group, tandem-repeat GALs, contains two distinct CRDs connected by a peptide linker, giving them molecular weights ranging from approximately 29–35 kDa. The third group consists of a single member, GAL-3, which has a molecular weight of approximately 26 to 30 kDa. GAL-3 contains a single CRD linked to a nonlectin N-terminal domain.

Although GALs have been shown to accomplish several intracellular and extracellular functions, they are best known for their immunoregulatory role.^{2–6} One of the hypotheses often raised to explain this immunoregulatory activity is that the proapoptotic activity of GALs on activated T cells is responsible, at

least in part, for the immunosuppression observed in the tumor microenvironment.^{7–10}

While the roles of GAL-1 and GAL-3 in cancer are well documented, GAL-7 has received less attention. This is mainly because GAL-1 and GAL-3 were identified first, and their expression is more ubiquitous than that of GAL-7, which is mostly found in stratified squamous epithelia, including tissues such as the skin, esophagus, tongue, trachea, and rectal mucosa.^{11–13} Its physiological role has been well documented in corneal injury repair, wound healing, and placentation, among others.^{13–16} In cancer, we and others have shown that cancer cells, including triple-negative breast cancer (TNBC), often express abnormally high levels of GAL-7.^{13,17–20} The specific role of GAL-7 can vary depending on the type of cancer, but it generally involves modulation of cell adhesion, apoptosis,

Received: January 9, 2025

Revised: March 25, 2025

Accepted: April 7, 2025

Published: April 10, 2025



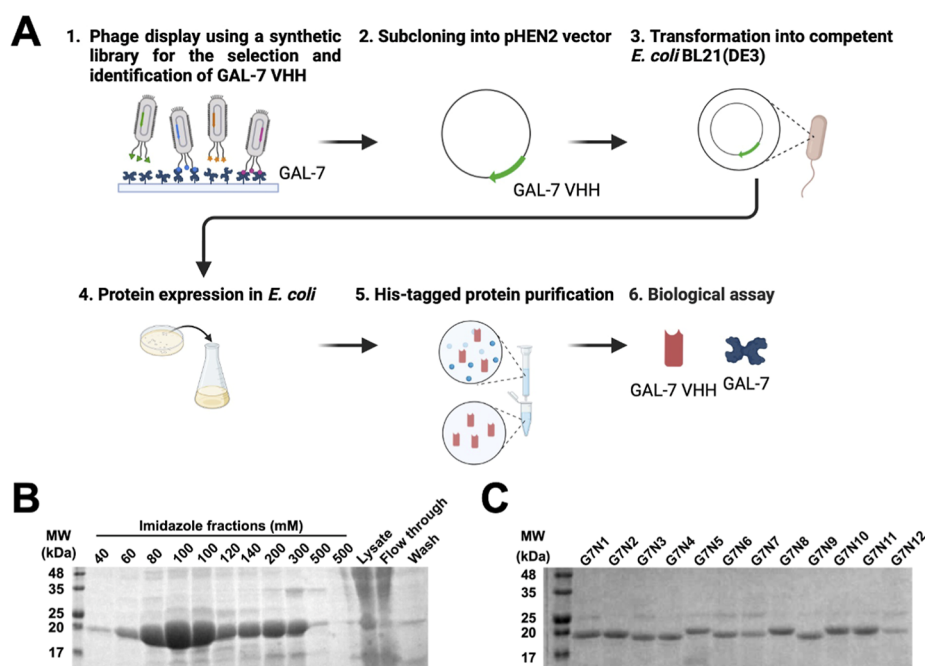


Figure 1. Generation, production, and purification of GAL-7 VHH. (A) Schematic representation of VHH selection using a synthetic library and production in *E. coli* expression systems. (B) SDS-PAGE analysis of the imidazole gradient following Nbs purification. (C) SDS-PAGE analysis of the 12 selected and purified VHHs. (B,C) Molecular weight (MW) markers are shown in kilodaltons (kDa). Results are representative of at least three independent experiments. Gel images were cropped for clarity.

Table 1. CDR Sequences of the 12 Nbs Targeting GAL-7^a

Nb	a.a.	MW (Da)	pI	CDR1	CDR2	CDR3
G7N1	181	19,672.52	5.71	TTSNSSG	WDHGIL	HGYVHFNMTHR---HISD
G7N2	175	19,273.06	5.31	RYSRIEI	STPSSN	R---WDWHS-----WDT
G7N3	175	18,629.40	5.29	AGSRDV	GFWGWWT	LLGAPCQTG-----
G7N4	175	18,940.69	5.07	RTSSQDI	DYSGGN	FLGEEKTS-----W
G7N5	178	19,632.54	5.45	DTSRFDV	WWSSDH	YGEYPPRMNR-----RP
G7N6	178	19,007.71	5.16	TTSNGEV	FGAGSS	ASWYHSSIG-----SMS
G7N7	169	18,190.74	5.03	GGYDWDA	SNNNGS	AD-----Q
G7N8	184	20,058.02	5.05	STSYSSST	FDGTSK	AGEWEALMNPVHDFWIY
G7N9	175	18,695.36	4.85	AYSFESG	SDADLF	A---FSSGG-----ELS
G7N10	184	20,067.05	5.61	STSYGET	YYSTRK	IVAYIYADGVRGYHQKID
G7N11	181	19,627.44	5.05	DTSESTS	RSSTWD	MADIFDNPQNASFMK---
G7N12	181	19,639.46	5.09	TYSSIEV	FEPNEF	SSVEWRQNGKPNATAS---

^aNb, nanobody; a.a., amino acids; MW, molecular weight; Da, Dalton; pI, isoelectric point; CDR, complementarity-determining region.

proliferation, and immune response. Emerging in vivo indications supports the hypothesis that GAL-7, like other GALs, may contribute to the establishment of an immunosuppressive microenvironment. For instance, Wu and colleagues have shown that GAL-7 depletes CD4⁺ T cells by binding to membrane-anchored PD-1.²¹ This is consistent with the work of An et al., which indicates that GAL-7 is released from tumor cells in vivo during the later stages of tumor development and that its expression is notably elevated in areas lacking CD8⁺ T cells.²² However, it is important to note that most current findings are based on models using knockout techniques or the administration of exogenous GAL-7, which do not fully replicate the complex interactions and concentrations of endogenously produced GAL-7 within the tumor microenvironment.

Given their critical role in cancer, considerable efforts have been directed toward the development of GAL inhibitors. However, despite nearly two decades of research, progress has been limited. In most cases, these inhibitors were high-

molecular-weight, naturally occurring polysaccharides or chemically modified glycans.²³ The most significant challenge in designing such inhibitors is achieving high selectivity, a formidable task given the striking structural similarity between the glycan-binding sites (GBS) of GALs, which has significant implications for off-target effects. Moreover, compelling evidence shows that GALs have noncarbohydrate-binding partners, particularly intracellular galectins, which perform crucial intracellular functions.^{2,24} Another obstacle to targeting GALs in cancer is the lack of noninvasive methods to detect the expression of GALs in primary tumors.

In this study, we used a synthetic naïve camelid single-domain antibodies (sdAb) phage library to generate high-affinity nanobodies (Nbs/VHH) that specifically target and inhibit GAL-7 functions. These Nbs show promising results for both tumor imaging and cancer treatment.

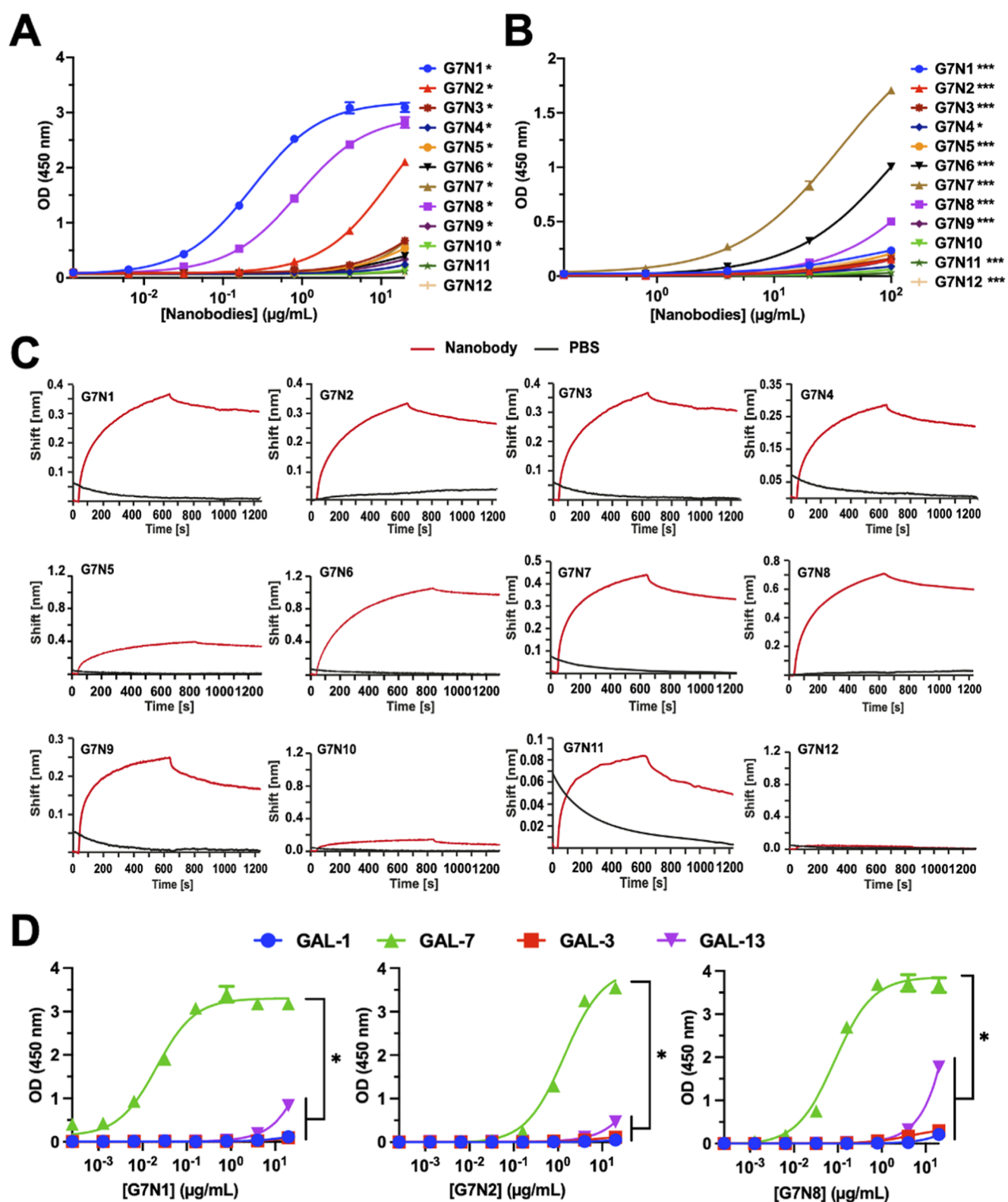


Figure 2. Binding affinity and specificity of Nbs to GAL-7 and other GALs. (A) Binding of Nbs to human GAL-7 directly coated on ELISA plates. $*P < 0.001$. (B) Binding of Nbs to GAL-7 bound to ASF-coated ELISA plates. $*P < 0.05$; $***P < 0.001$. (C) BLI analysis of Nbs binding to GAL-7. (D) Binding of lead Nbs (G7N1, G7N2, and G7N8) to GAL-1, GAL-3, GAL-7, and GAL-13, measured by ELISA. $*P < 0.001$. (A–D) Results are representative of at least three independent experiments. (A,B,D) Data are presented as mean \pm standard deviation (SD). Analyses were performed using one-way ANOVA followed by Dunnett's multiple comparisons test and statistical significance was assessed at the highest tested concentration for each experiment.

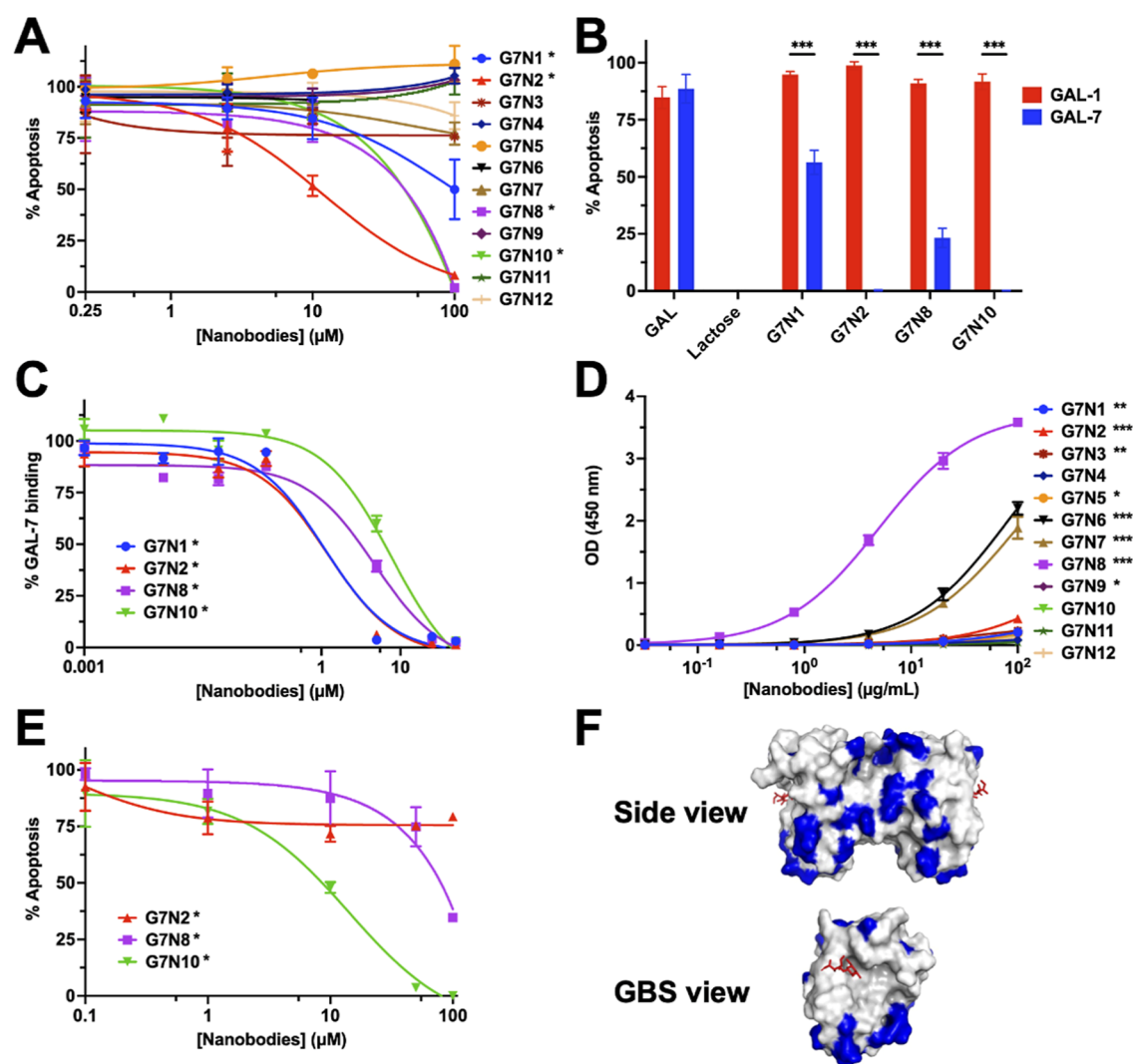


Figure 3. Characterization of Nbs and cross-reactivity with mouse GAL-7. (A) Dose–response inhibition of GAL-7-induced apoptosis of Jurkat T cells by the 12 Nbs. $*P < 0.05$ by two-tailed *t*-test. (B) Apoptosis of Jurkat T cells induced by human GAL-1 or GAL-7 preincubated with lead Nbs (G7N1, G7N2, G7N8, and G7N10) at 50 μM . Controls include cells incubated with GAL-1 or GAL-7 alone (GAL) and with lactose as a positive inhibition control. $***P < 0.001$ by two-way ANOVA. (C) Dose–response inhibition of FITC-labeled GAL-7 binding to Jurkat cells after preincubation with the lead Nbs (G7N1, G7N2, G7N8, and G7N10). $*P < 0.001$ by two-tailed *t*-test. (D) Binding of the 12 Nbs to mouse GAL-7, as measured by ELISA. $*P < 0.05$; $**P < 0.01$; $***P < 0.001$ by one-way ANOVA, followed by Dunnett’s multiple comparisons test. (E) Dose–response inhibition of mouse GAL-7-induced apoptosis of Jurkat T cells by the selected lead Nbs G7N2, G7N8 and G7N10. $*P < 0.001$ by one-way ANOVA, followed by Dunnett’s multiple comparisons test. (A–E) Results are representative of three independent experiments. Data are presented as mean \pm SD (A,C–E) Statistical significance was assessed at the highest tested concentration for each experiment. (F) Structural comparison between human and mouse GAL-7. Differences in primary structure are mapped onto the 3D structure of human GAL-7 (PDB 2GAL). Identical residues between mice and human GAL-7 are shown in white, while distinct residues are colored blue. Galactose molecules in the GBS are shown as red sticks. Most primary structure differences are observed at the dimer interface, while the GBS environment is largely identical in both proteins.

RESULTS

Generation and Characterization of GAL-7 Nbs. Nbs were generated following three rounds of selection on Hybrigenics’ synthetic hsd2Ab VHH library consisting of 3×10^9 clones expressed at the surface of M13 phages, as previously described²⁵ (Figure 1A). Selection was performed using biotinylated GAL-7, allowing the identification of Nbs that recognize the nonadsorbed antigen in its native form. A total of 462 VHHs were randomly selected and analyzed after three rounds. The 12 best clones were retained after validation by enzyme-linked immunosorbent assay (ELISA). Sequencing analyses of the CDR1 and CDR2 regions of the Nbs showed that they were encoded by short sequences of 6–8 amino acids (Table 1). In contrast, significant structural variability was

observed for the CDR3 loop, which showed a much broader distribution in length (3–18 amino acids).

The 12 selected clones were subcloned into the pHEN2 vector for expression in *Escherichia coli* (*E. coli*) and purified using standard His-tag purification protocols (Figure 1B,C). Nbs were first tested for their ability to bind human GAL-7, which was immobilized either by passive adsorption on ELISA plates or on asialofetuin (ASF) (Figure 2A,B). Our results demonstrated that several Nbs bound to GAL-7 at the tested concentrations. Specifically, G7N1, G7N2, and G7N8 showed the strongest binding to GAL-7 directly coated onto ELISA wells, while G7N6, G7N7, and G7N8 showed the strongest binding to GAL-7 immobilized on ASF (Figure 2A,B). Further evidence of Nbs binding to human GAL-7 was obtained by

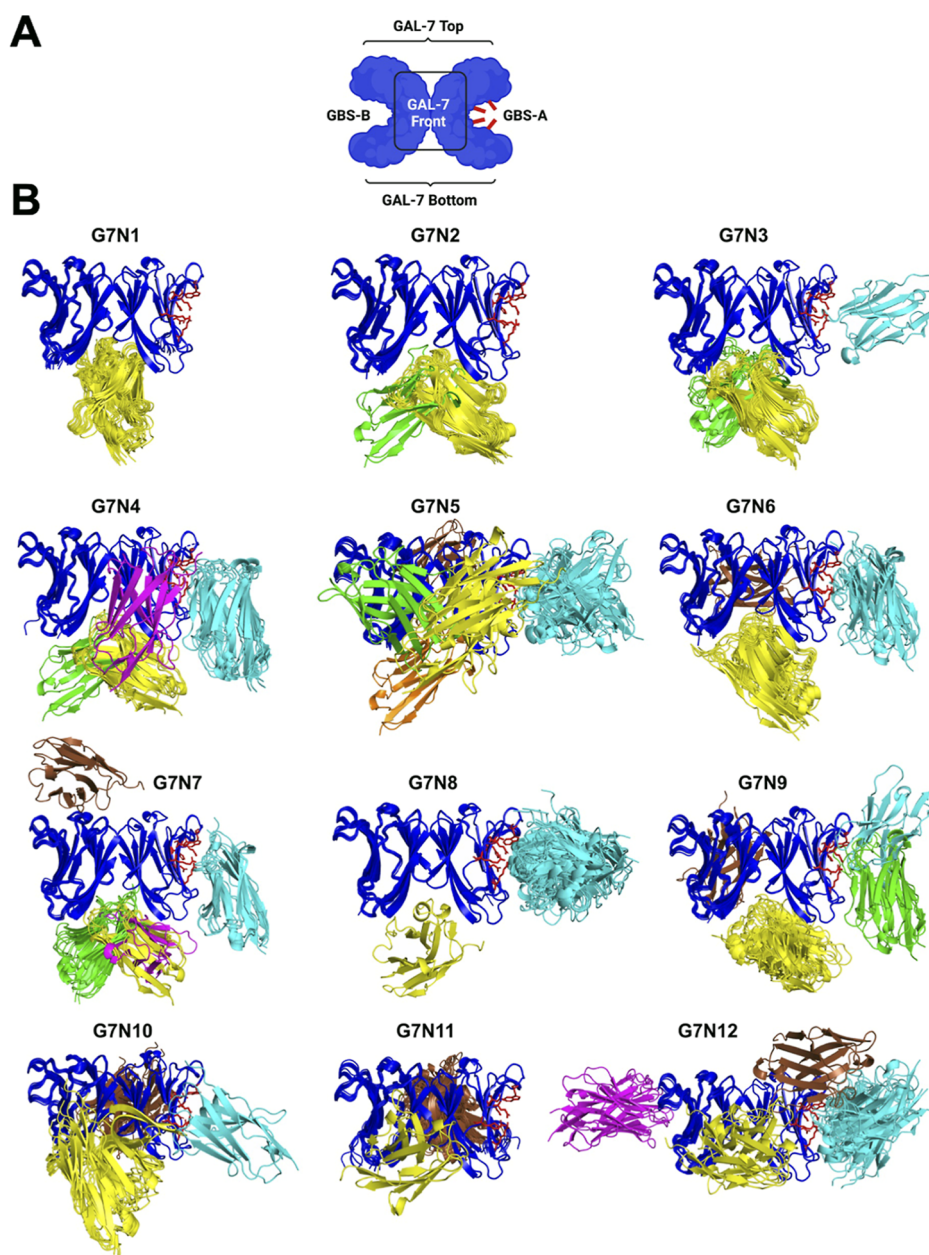


Figure 4. AlphaFold3-predicted epitopes targeted by the 12 Nbs on the surface of the GAL-7 homodimer. All AlphaFold3 predictions confirmed the expected back-to-back homodimer architecture of GAL-7 (dark blue), consistent with its crystal structure. The 12 distinct Nbs were found to bind different epitopes on the surface of GAL-7, with preferred sites determined from statistical analysis of 120 independent predictions (see the Experimental section for details). (A) Schematic side-view representation of a GAL-7 homodimer (dark blue), with GBS residues of protomer A shown as red sticks. The preferred Nb binding epitopes on the surface of GAL-7 clustered into six primary regions, ranked by occurrence (Table 2): (1) at the bottom of the GAL-7 dimer interface (54/120 predictions), (2) near the GBS of protomer A (34/120), (3) in front of the GAL-7 homodimer (13/120), (4) at the back of the GAL-7 homodimer (15/120), and (5) near the GBS of protomer B (2/120). (B) AlphaFold3-predicted formation of structural complexes between GAL-7 and the 12 individual Nbs. Each panel displays an overlay of 10 distinct AlphaFold3 predictions. The GAL-7 homodimer is shown in blue, with GBS residues of protomer A in red sticks. For clarity, Nb binding predictions with distinct orientations and/or unique GAL-7 epitopes are color-coded differently in each panel (yellow, green, cyan, orange, magenta, brown), though colors are not consistent across panels. Some Nbs exhibit highly consistent and reproducible binding predictions (e.g., G7N1, G7N2, and G7N8), while other Nbs randomly scatter across multiple epitopes on the surface of GAL-7 (e.g., G7N5, and G7N12).

biolayer interferometry (BLI) (Figure 2C). Except for G7N12, all Nbs exhibited a similar association curve. Notably, G7N8 generated a stronger signal, which aligned with our ELISA data. Importantly, we assessed the specificity of the lead Nbs G7N1, G7N2, and G7N8 for GAL-7 in comparison to GAL-1 and GAL-3, which are commonly coexpressed with GAL-7 in cancer tissues^{26–29} (Figure 2D). The results demonstrated significant stronger binding to GAL-7 over GAL-1, GAL-3, and GAL-13.

Inhibition of GAL-7-Induced Apoptosis. Extracellular GALs, including GAL-7, are well-known for their ability to induce apoptosis of activated T cells. To assess whether our Nbs could inhibit GAL-7-induced apoptosis, we used Jurkat T cells, a well-established *in vitro* model to study GAL-induced apoptosis.^{30–33} Jurkat T cells were incubated with recombinant human GAL-7 alone or with increasing concentrations of the 12 Nbs. T cell apoptosis was measured by flow cytometry using

standard annexin V/propidium iodide (PI) staining. Our results showed that among the 12 Nbs, G7N1, G7N2, G7N8, and G7N10 were the most potent (Figure 3A). The inhibition of GAL-7-induced apoptosis was highly specific, as no significant inhibition was observed in GAL-1-induced apoptosis with the lead Nbs (G7N1, G7N2, G7N8, and G7N10) (Figure 3B). Our results suggest that this inhibition of apoptosis is likely due to the ability of the Nbs to prevent GAL-7 from binding to T cell surface receptors (Figure 3C). Furthermore, we confirmed that the binding of three selected lead Nbs (G7N1, G7N2, and G7N8) to GAL-7 was not inhibited by lactose or *N*-acetylglucosamine (LacNAc) (Supporting Information Figure S1A). Because the ability of the Nbs to bind the mouse target is crucial for understanding its mechanism of action, such as immune effector functions or receptor signaling, we next evaluated whether the generated Nbs could bind to the mouse homologue of GAL-7 (Figure 3D). Most notably, G7N8 showed the strongest binding to mouse GAL-7 and inhibited Jurkat apoptosis induced by mouse GAL-7 (Figure 3D,E).

G7N8 Primarily Binds to the GBS Environment of GAL-7. To better understand the mechanism of action of our lead Nb, G7N8, and its ability to modulate the activity of both human and mouse GAL-7, we acquired and compared nuclear magnetic resonance (NMR) ^1H - ^{15}N HSQC spectra of free GAL-7 and GAL-7 in complex with G7N8. These NMR experiments measure local atomic-scale perturbations in GAL-7 residues upon G7N8 binding, allowing us to experimentally validate which GAL-7 residues are involved in the formation of the GAL-7/G7N8 protein–protein complex.

Our NMR results illustrate that the primary residues targeted by G7N8 on the surface of GAL-7 are located near the GBS, forming a preferred epitope within this functional environment (Supporting Information Figure S1B). Targeting residues near the GBS in human GAL-7 also provides a plausible explanation for the dual binding affinity of G7N8 to mouse GAL-7. Indeed, comparative surface analysis between human GAL-7 and mouse GAL-7 shows that both proteins share a nearly identical sequence and structural epitope in their GBS environment, in contrast to significant sequence variations near their dimer interface (Figure 3F). Combined with AlphaFold3 structural predictions performed with other Nbs (see below), these results may explain why Nbs that primarily target the dimer interface of GAL-7 (e.g., G7N1, G7N2) do not exhibit the same dual affinity and functional modulation between the mouse and human GAL-7 homologues.

AlphaFold3 Structural Predictions of GAL-7/Nbs Interactions. Given that Nbs distinctively inhibit apoptosis and exhibit significant binding heterogeneity, we hypothesized that they likely have distinct mechanisms of action and target unique epitopes on the surface of GAL-7. To investigate this, we used AlphaFold3, an advanced artificial intelligence model that significantly improves predictions of protein interactions with other biological molecules.³⁴

GAL-7 is biologically active as a homodimer and also crystallizes in this form (e.g., PDB entry 1BKZ). In contrast, Nbs are sdAb active in their monomeric state, often serving as crystallization chaperones.³⁵ To investigate complex formation and determine the most probable Nb binding epitopes on the surface of GAL-7, we used AlphaFold3 to predict hetero-complexes between GAL-7 and each individual Nb (G7N1 to G7N12). These predicted structures provide an overall framework for understanding the most likely higher-order architectures formed between these protein partners, offering

further insight into the distinct mechanisms of action of each Nb. Our results showed that all 12 GAL-7/Nbs complexes predicted by AlphaFold3 accurately validated the experimental 3D architecture of GAL-7, maintaining a conserved homodimeric GAL-7 structure bound to a single monomeric Nb (Figure 4A,B). These results are supported by very high pLDDT scores (>90) for the respective protein cores of the GAL-7 homodimer and Nb monomer. As expected, lower confidence metrics were primarily concentrated in Nb loops that form the CDR1, CDR2, and CDR3 variable regions, which are surface-exposed and flexible paratopes.

Predictions of GAL-7/Nbs complexes also yielded respectable template modeling (pTM) and interface predicted template modeling (ipTM) scores, which measure the accuracy of the entire structure.^{36,37} pTM and ipTM scores for the top-ranked prediction in each of the 5-seed runs are presented in Table 2.

Table 2. AlphaFold3 Predictions of GAL-7/Nbs Complex Formation

Nb	ipTM/pTM	Preferred Nb target epitopes on the surface of the GAL-7 homodimer				
		GBS-A	bottom	front	back	top
G7N1	0.61/0.72 0.68/0.77	0	10	0	0	0
G7N2	0.74/0.81 0.60/0.72	0	10	0	0	0
G7N3	0.48/0.64 0.49/0.65	1	9	0	0	0
G7N4	0.52/0.66 0.51/0.66	4	5	1	0	0
G7N5	0.49/0.65 0.48/0.64	5	1	3	1	0
G7N6	0.47/0.63 0.51/0.66	3	6	0	1	0
G7N7	0.60/0.72 0.53/0.68	3	6	0	0	1
G7N8	0.48/0.64 0.48/0.64	9	1	0	0	0
G7N9	0.50/0.65 0.50/0.65	3	6	0	1	0
G7N10	0.43/0.61 0.46/0.63	1	0	6	3	0
G7N11	0.51/0.66 0.53/0.67	0	0	1	9	0
G7N12	0.46/0.63 0.45/0.62	7 ^a	0	2	0	1

^a5 hits in GBS of protomer A and 2 hits in GBS of protomer B. Nb, nanobody; ipTM, interface predicted template modeling; pTM, predicted template modeling; GBS, glycan-binding site.

pTM values are well above 0.6, suggesting that the overall predicted fold of the complexes is likely similar to the true structure. However, significant variability was observed in the preferred binding sites for the 12 Nbs (Figure 4). This binding heterogeneity is likely reflected by lower ipTM scores, which measure the accuracy of the predicted relative positions of the subunits within the complex.

It would be presumptuous to assume that AlphaFold3-predicted structures of all GAL-7/Nbs complexes illustrate their exact atomic positioning. However, the comparative binding site analysis between distinct Nbs provides key molecular information regarding preferred target epitopes on the surface

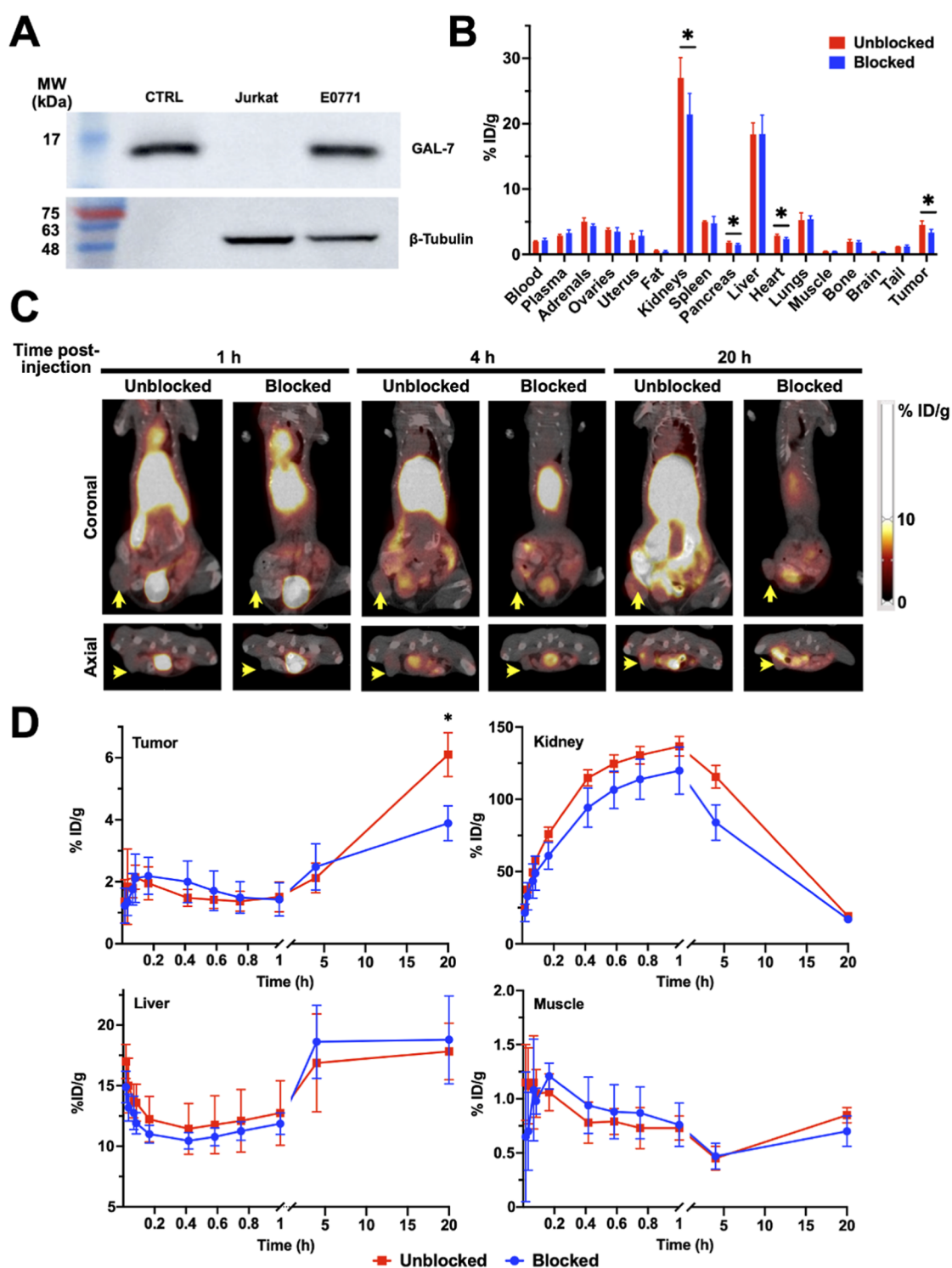


Figure 5. *In vivo* and *ex vivo* distribution of $[^{64}\text{Cu}]\text{Cu-NOTA-G7N8}$ and PET imaging in a TNBC mouse model overexpressing GAL-7. (A) GAL-7 expression in E0771 cells was analyzed by Western blot (captured image was cropped). Recombinant GAL-7 was used as a positive control (CTRL), and Jurkat cells were used as a negative control. (B) Biodistribution of $[^{64}\text{Cu}]\text{Cu-NOTA-G7N8}$ in unblocked and blocked mice (coinjection of 17 nmol cold G7N8) at 20 h postinjection ($n = 4$ for unblocked mice and $n = 6$ for blocked mice). * $P < 0.05$ by two-tailed t -test. (C) Axial and coronal views of mice showing the accumulation of $[^{64}\text{Cu}]\text{Cu-NOTA-G7N8}$ in unblocked and blocked mice (coinjection of cold G7N8 at 17 nmol) at 1, 4, and 20 h postinjection. Arrows indicate E0771 tumors. (D) Time-activity curves of unblocked and blocked $[^{64}\text{Cu}]\text{Cu-NOTA-G7N8}$ in the tumor, kidney, liver, and muscle. * $P < 0.001$ by two-tailed t -test. (B,D) Data are presented as mean \pm SD.

of GAL-7. Indeed, we identified 6 primary epitopes on the GAL-7 homodimer, with preferred Nb binding sites located at the bottom of the GAL-7 dimer interface (54/120 predicted structures) and within the GBS of protomer A (34/120)

(Table 2, Figure 4B). Fewer predictions favored Nb binding to the front (13/120) or back (15/120) of the GAL-7 dimer, and only two predictions targeted the GBS of protomer B. These latter results illustrate differences in GBS geometry between

protomers A and B within the apo GAL-7 homodimer structure. They further support previously observed long-range effects, suggesting positive cooperativity and allosteric communication upon ligand binding to this scaffold.^{38,39}

Interestingly, our experimental results strongly correlate with the consistency of AlphaFold3 structural models. Although some Nbs (e.g., G7N5 and G7N12) are predicted to randomly scatter across multiple epitopes on the surface of GAL-7, our most potent Nbs (G7N1, G7N2, and G7N8) are consistently predicted by AlphaFold3 to bind specific epitopes on GAL-7 (Figure 4B). Indeed, while G7N1 and G7N2 both appear to selectively target the bottom interface of the GAL-7 dimer (10/10 predicted structures each), our lead Nb, G7N8, is predicted to bind within the GBS environment of GAL-7 (9/10 structures). Among the 12 Nbs, G7N8 is the only to systematically favor binding to the GBS, which may explain its unique molecular properties. This observation further illustrates how the most potent Nbs, G7N1, G7N2, and G7N8, likely act through distinct molecular mechanisms of action when targeting GAL-7. In summary, AlphaFold3 structural predictions offer essential insights that enhance our understanding and enable the optimal use of our 12 Nbs as molecular tools to investigate the biological functions of GAL-7.

GAL-7-Specific Nbs for Imaging. To our knowledge, there is currently no noninvasive research or clinical imaging tools to detect the presence of GALs in primary tumors. Because Nbs are considered very promising for noninvasive imaging, especially for cancer detection, we explored the possibility of using G7N8 to detect GAL-7 accumulation in a solid tumor. Given that GAL-7, like other GALs, is known to modulate antitumor immune response, we used an immunocompetent syngeneic model, in this case E0771 cells implanted in C57BL/6 mice. This model is well established for preclinical studies of TNBC, a cancer subtype known to express abnormally high levels of GAL-7.⁴⁰ As observed in humans, E0771 cells constitutively express GAL-7 (Figure 5A). We developed [⁶⁴Cu]Cu-NOTA-G7N8 and evaluated its stability, biodistribution, and pharmacokinetics by positron emission tomography (PET) imaging in E0771 tumor-bearing mice. The 1,4,7-triazacyclononane-1,4,7-triacetic acid (NOTA) conjugation yield was 76%, and the average number of NOTA per G7N8, measured using an isotopic dilution assay, was 0.9 ± 0.3 . NOTA-G7N8 was subsequently labeled with [⁶⁴Cu]Cu with a radiolabeling yield of 99% and an apparent specific activity of 0.78 ± 0.11 GBq/mg (Supporting Information Table S1 and Figure S2). The half-life of [⁶⁴Cu]Cu matches well with the biological half-life of Nbs. By PET/CT imaging, we observed an optimal tumor uptake at 20 h after administration of [⁶⁴Cu]Cu-NOTA-G7N8 (Figure 5B–D). The tumor uptake decreased when mice were coinjected with an excess of G7N8 (Figure 5B,D). We also observed high accumulation of [⁶⁴Cu]Cu-NOTA-G7N8 in the kidneys, followed by renal-urinary clearance after 20 h (Figure 5C,D). On the other hand, liver accumulation was observed over 20 h postinjection, possibly due to the *trans*-chelation of [⁶⁴Cu]Cu to liver proteins. Ex vivo distribution studies also showed significant differences in tumor uptake values between unblocked and blocked mice at 20 h postinjection, as well as in kidneys and, to a lesser extent, the pancreas and heart (Figure 5B).

DISCUSSION AND CONCLUSIONS

Given the critical role of GALs in many diseases, considerable efforts have been made to develop specific GAL inhibitors for

research purposes and therapeutic applications. In the present work, we report the successful generation of specific and potent Nbs targeting human GAL-7, a member of the GALs family involved in tumor progression of many cancers, including aggressive subtypes of breast cancer such as TNBC. We generated 12 Nbs, among which G7N1, G7N2, G7N8, and G7N10 were particularly potent in inhibiting GAL-7-induced apoptosis of human T cells. Notwithstanding the potential of these Nbs to inhibit the biological functions of GAL-7, we leveraged the cross-reactivity of G7N8 with mouse and human GAL-7 to study the possibility of detecting tumors expressing GAL-7 by PET/CT imaging. Our results with [⁶⁴Cu]Cu-NOTA-G7N8 are promising and hold out the prospect of 1 day using these Nbs for diagnostic and theranostic purposes. GAL-7, like most GALs, is predominantly expressed in the cytoplasm of cancer cells and is passively released into the extracellular space. Our results demonstrate Nbs can effectively detect GAL-7 in the tumor microenvironment. Of course, this approach remains to be optimized before this tracer can be used in the clinic. There are many ways to optimize the pharmacokinetic properties of Nbs to make them better detection agents, whether by modifying surface charges, pegylation, and other ways.⁴¹ Particular attention should be given to reducing nonspecific accumulation in the liver. Interestingly, our results measuring ex vivo biodistribution confirmed that the constitutive expression of GAL-7 in human tissues is minimal. Expression in the pancreas, although low, aligns with previous findings indicating that human pancreatic cells express GAL-7.⁴² Our results open the possibility of targeting pancreatic cancer with Nbs against GAL-7. These findings also open new opportunities for developing theranostic applications for diseases where GAL-7 plays a central role, including high-fatality cancers.^{43,44} Nanobodies are emerging as valuable imaging tools for stratification of cancer patients. Because of their small size, they are particularly effective at penetrating solid tumors and providing important information to clinicians. A case in point is detecting a PD-L1 positive tumor, enabling the identification of patients likely to respond to immune checkpoint inhibitors.^{45–47} We thus foresee the use of G7N8 to identify patients who respond to specific treatments, particularly in TNBC, where GAL-7 expression varies among tumors. Additionally, G7N8 could confirm GAL-7 presence in other cancer types, paving the way for the development of GAL-7-targeted therapies.

Therapeutically, GAL-specific Nbs can be used as neutralizing agents, like a receptor–ligand antagonist, or a vehicle for effector delivery and targeted drug therapy. The therapeutic potential of camelid sdAb for treating diseases is a rapidly evolving field.⁴⁸ In addition to their small size, which makes them highly efficient for noninvasive imaging, the fact that Nbs can be produced in cost-effective large-scale bacterial production systems and that they are known for their low immunogenicity makes them attractive as research tools and for therapeutic applications. Moreover, the biochemical and structural properties of Nbs confer them with high versatility.⁴⁹ For example, Nbs against PD-L1 can be adapted for chimeric antigen receptor (CAR) T cell therapy.⁵⁰ They can also easily be used to generate minibodies by fusing the Nb to a human IgG1 framework, thereby extending their in vivo half-life while enabling antibody-dependent cell-mediated cytotoxicity (ADCC) and complement-dependent cytotoxicity (CDC). The resulting multivalent construct may enhance avidity toward the target antigen, leading to improved target binding and potentially greater biological activity. Another interesting advantage of Nbs is their potential application in

blocking intracellular functions. This is an important issue in the case of GALs, which perform diverse intracellular functions.²⁴ For example, Nbs have been recently used as intrabody homologues to block protein kinase activity in human cells.⁵¹ This opens the way to new strategies to target the intracellular functions of galectins, a challenge historically difficult to overcome with traditional inhibitors. These intrabodies could either inhibit certain specific actions by targeting distinct epitopes or facilitate the degradation of intracellular galectins, similar to protein knockdown.

Our results suggest that our Nbs bind to sites that are topographically distinct from the GBS and likely act via entirely different mechanisms of action. This represents another advantage when compared to traditional GAL inhibitors. There is compelling evidence that GALs, including GAL-7, interact with noncarbohydrate binding partners.^{52–56} Such GBS-independent functions represent a paradigm shift in our understanding of the biology of GALs and the development of GAL-targeted therapeutics. Although our hierarchical validation pipeline focused on inhibiting GAL-7-induced apoptosis, such a pipeline could be easily modified to target other biological activities of GAL-7 or its interactions with specific ligands, including intracellular ligands, as discussed above, using our modeling data as a starting point. However, future studies will be necessary to validate the modeling data predicted by AlphaFold3. Our results thus open an entirely new area for research into the fundamental roles of GAL-7 and its therapeutic potential across various diseases.

Our study paves the way for the development of Nbs targeting other GAL family members. This is an important issue, most notably for those less well-known GALs and their involvement in unexpected diseases, using an out-of-the-box approach.⁵⁷ Finally, from a methodological perspective, our study further supports that synthetic libraries are suitable for generating GAL-specific neutralizing Nbs and do not require the construction of immune libraries. Moreover, if needed, it is also possible to use directed evolution in vitro maturation techniques to improve the affinity of a given Nb or modify their specificity.

In summary, our study provides a proof-of-concept for a novel generation of inhibitors targeting GAL family members. It also introduces a new set of research tools to better understand the biological roles of GALs, most notably those whose cellular functions remain elusive.

■ EXPERIMENTAL SECTION

General Procedures. All proteins were expressed in *E. coli* BL21(DE3) cells and purified using affinity chromatography. In vitro biological and binding assays were conducted using various methods to characterize the specificity and efficacy of Nbs, including ELISA, BLI, flow cytometry, and NMR spectroscopy. Western blot was performed to verify GAL-7 expression in cell lines for in vivo assays. Structural predictions of GAL-7/Nbs complexes were determined using AlphaFold3. For in vivo and ex vivo assays, G7N8 was conjugated to NOTA and radiolabeled with copper-64 acetate [⁶⁴Cu]Cu(OAc)₂. [⁶⁴Cu]Cu-NOTA-G7N8 was administered to female C57BL/6 TNBC-bearing mice. The plasma stability of the radiolabeled compounds was evaluated using radio-thin layer chromatography (radio-TLC) on a C18 plate. PET imaging was performed using LabPET 8 scanner and biodistribution across different tissues was assessed using a gamma counter.

Production and Purification of Recombinant GALs. Codon-optimized vectors encoding human and mouse GALs were cloned into pET-22b(+). GAL-1, GAL-3, and GAL-7 were purified using standard lactose affinity chromatography, as previously described.³⁰ Human GAL-13 was produced using the same expression system but purified by

affinity chromatography on a mannose column (Sigma) and eluted with a NaCl gradient in 50 mM Tris buffer.

Generation of Nbs. GAL-7-specific Nbs were generated by Hybrigenics. A synthetic library of humanized Nbs was screened against biotinylated recombinant full-length human GAL-7 protein. After three rounds of selection, VHH clones were randomly selected and tested using a nonabsorbed phage ELISA assay with avidin-coated plates and biotinylated-GAL-7 antigen for cross-validation. Twelve clones were identified based on their amino acid sequences, and their cDNA was cloned into the pHEN2 expression vector, as previously described.²⁵

Production and Purification of Nbs. Competent *E. coli* BL21(DE3) cells were transformed with pHEN2 constructs, and expression of Nbs was induced as previously described.²⁵ Nbs were purified from the cell lysate using standard immobilized metal affinity chromatography with prepacked Cytiva His GraviTrap columns (Sigma) and eluted with an imidazole gradient. Purified Nbs were dialyzed in phosphate-buffered saline (PBS) to remove imidazole.

ELISA Assay. For ELISA, human recombinant GAL-1, GAL-3, GAL-7, GAL-13, mouse GAL-1, and mouse GAL-7 were diluted to 10 μg/mL in PBS and coated onto flat-bottom 96-well polystyrene plates (Costar) for 1 h at room temperature (RT). After washing with PBS, wells were blocked with PBS/1% bovine serum albumin (PBA) for 1 h at RT. Following washes, Nbs were diluted at indicated concentrations in PBA and incubated for 1 h at RT. The binding of Nbs was measured by direct ELISA using HRP anti-Myc tag antibody (cat.: ab62928; Abcam), incubated for 1 h at RT (1:10,000 dilution in PBA). After washes, 3,3',5,5'-tetramethylbenzidine (TMB) liquid substrate system (Sigma) was added. The reaction was stopped after 30 min with 0.16 M sulfuric acid. Absorbance at 450 nm was measured using a Tecan plate reader. This protocol was also used for ELISA with human recombinant GAL-7 immobilized on ASF. Briefly, ASF was coated at 1 μg/mL in carbonate-bicarbonate buffer (pH 9.2) overnight at 4 °C. After blocking with PBA, 10 μg/mL of GAL-7 was added to wells for 1 h at RT.

BLI Analysis. Binding analysis of GAL-7 was performed using BLI with ForteBio Octet K2 (Pall ForteBio). Recombinant GAL-7 (10 μg/mL) was immobilized on AR2G2 sensors, which were subsequently incubated with Nbs (40 μg/mL) and PBS as a negative control.

Apoptosis Assay. Apoptosis was measured by flow cytometry using FITC Annexin V (cat.: 640906; Biologend) and PI (cat.: P4170; Sigma). Jurkat T cells were treated for 4 h at 37 °C with 15 μM of GAL-7 or 2.5 μM of GAL-1, preincubated with or without Nbs overnight at 4 °C. After incubation, cells were washed with binding buffer (0.01 M HEPES, 0.14 M NaCl, 2.5 mM CaCl₂, pH 7.4) and centrifuged. Cell pellets were resuspended and incubated with FITC-labeled Annexin V (0.63 μg/mL) for 15 min at RT in the dark. PI (0.25 μg/mL) was added to cells prior to flow cytometry analysis, which was carried out on a FACSCalibur flow cytometer (BD Biosciences). 5000 events were recorded for each sample.

Binding Assay. GAL-7 was conjugated with FITC using standard method. To test the inhibition of GAL-7 binding to Jurkat cells, 2 μM of FITC-conjugated GAL-7 was preincubated with 5 μM or 25 μM of lead Nbs G7N1, G7N2, G7N8, or G7N10 and PBS (negative control) or 100 mM of lactose (positive control) overnight at 4 °C. After preincubation, Jurkat cells were incubated with the indicated conditions for 30 min at 4 °C. The samples were analyzed using a FACSCalibur flow cytometer (BD Biosciences).

NMR Spectroscopy. ¹⁵N-labeled human GAL-7 was expressed and purified as previously described.³⁸ The ¹⁵N-GAL-7/G7N8 complex was prepared by preincubating 200 μM of each protein in 50 mM Tris, 150 mM NaCl (pH 8.0) at 45 °C for 5 h to achieve a stoichiometric ratio of 1:2 of dimeric GAL-7 to G7N8. To study the unbound protein, ¹⁵N-GAL-7 was preincubated alone under the same conditions. ¹H–¹⁵N HSQC spectra were acquired on a Bruker AVANCE III spectrometer at a working ¹H frequency of 600 MHz, equipped with a 5 mm QCIQF helium cryoprobe. Spectra were processed and analyzed using Bruker Topspin v3.5pL7 and CcpNmr AnalysisAssign v2.4.⁵⁸ Backbone NMR chemical shift assignments for ¹⁵N-GAL-7 were obtained from the Biological Magnetic Resonance Bank (BMRB Entry 17826) and adjusted according to the different buffer conditions, with only minor

changes observed. Chemical shift variations are a composite of amide ^1H and ^{15}N chemical shift values calculated according to the relationship $\Delta\delta = [(\delta_{\text{HN}}^2 + (\delta_{\text{N}}/5)^2)/2]^{1/2}$, in which $\Delta\delta$ is the difference in the chemical shift between free and G7N8-bound ^{15}N -GAL-7 for amide $^1\text{H}^{\text{N}}$ and $^{15}\text{N}^{\text{H}}$ nuclei.^{59,60}

AlphaFold3 Structural Predictions. The formation of the complex between GAL-7 and Nbs was predicted using two independent GAL-7 monomers and one Nb monomer as input sequences, with the default parameters of the AlphaFold3 server.³⁴ All 12 Nbs were subjected to two independent AlphaFold3 runs against GAL-7, generating five individual predictions per run, resulting in 10 independent GAL-7/Nb complexes per Nb. The pTM and ipTM scores for the top-ranked predictions in each 5-seed run are presented in Table 2. All Nb models were structurally overlaid using the GAL-7 protomer A as a target and analyzed using the open-source PyMOL Molecular Graphics System, Version 2.5.0.

Cell Culture. E0771 and Jurkat cells were maintained at 37 °C, with high humidity and 5% CO_2 . Jurkat cells were cultured in RPMI 1640 medium and E0771 cells in DMEM, both supplemented with 10% [v/v] fetal bovine serum (FBS). Cell lines were purchased from the American Type Culture Collection (ATCC).

Western Blot Analysis. Cells were lysed in radioimmunoprecipitation assay (RIPA) buffer with phenylmethylsulfonyl fluoride (PMSF) as a protease inhibitor for 30 min at 4 °C. Lysates were centrifuged at 15,000g for 15 min at 4 °C. Protein lysates were resolved by SDS-PAGE and transferred to PVDF membranes (Bio-Rad) by electroblotting at 100 V for 1 h. PVDF membranes was blocked using PBS buffer with 5% (w/v) nonfat dry milk and 0.1% (v/v) Tween-20. The primary antibodies, human anti-GAL-7 (cat.: AF1339; R&D Systems) and anti- β -tubulin (cat.: 2128; Cell Signaling Technology), were incubated overnight at 4 °C. After washing, membranes were incubated with HRP-conjugated secondary antibodies for 1 h at RT. Detection was performed using ECL Western Blotting Detection Reagents (Cytiva) and ImageQuant LAS 500.

NOTA Conjugation. Conjugation of G7N8 with NOTA was carried out using a 10-fold excess of NOTA-NHS in 0.1 M sodium bicarbonate buffer, pH 9.0, at room temperature for 2 h. The purification was performed by ultrafiltration (Centriprep, 3000 Da) at 8000 rpm for 10 min with 500 μL of trace-metal free PBS (pH 7.4) (5 \times). Protein concentration was measured using a BCA protein assay.⁵¹ The number of NOTA was determined by isotopic dilution after [^{64}Cu]Cu labeling, using the method described by Meares et al.⁶²

Radiolabeling of NOTA-G7N8. Copper-64 acetate [^{64}Cu]Cu-(OAc)₂ was prepared at the Centre d'imagerie moléculaire de Sherbrooke (CIMS). For labeling, 25 nM of NOTA-G7N8 was added to 390 MBq of [^{64}Cu]Cu(OAc)₂ in 0.1 M ammonium acetate buffer (pH 5.5) for a final volume of 400–500 μL and was incubated at room temperature for 20 min. The reaction was followed by radio-TLC using C18 plates and 0.1 M sodium citrate pH 5.5 as eluent. In this system, the free [^{64}Cu]Cu migrated with the solvent front, while [^{64}Cu]Cu-NOTA-G7N8 remained at the origin. The radiotracer was used without further purification.

Animal Model. Female C57BL/6 mice (6–8 weeks old) were purchased from Charles River Laboratories and were housed in sterile cages, maintained in a temperature-controlled room with *ad libitum* access to water and food. For orthotopic tumor implantation, E0771 tumor cells (1×10^6 cells/mouse) were injected into the fourth mammary fat pad. Mice were monitored daily for signs of disease and end point criteria. All experiments were conducted following a protocol approved by the Animal Ethics Committee of Université de Sherbrooke and complied with the Canadian Council on Animal Care guidelines (Protocol ID—2022–3704R). All procedures that could cause pain, stress, or immobilization were performed under isoflurane anesthesia (2% in 2 L/min oxygen) with a heating pad or bed. Euthanasia was performed by CO_2 inhalation under isoflurane anesthesia when required.

Plasma Stability of [^{64}Cu]Cu-NOTA-G7N8. Plasma stability analysis was conducted by incubating [^{64}Cu]Cu-NOTA-G7N8 (100 MBq in 250 μL PBS) with 250 μL of mouse plasma at 37 °C for 24 h. The plasma was then mixed with 500 μL of pure acetonitrile to

precipitate proteins. A 1 mL aliquot was transferred into two ultra-15 centrifugal filter units (30 kDa), followed by ultrafiltration at 8000 rpm for 20 min. The filtrate with [^{64}Cu]Cu-NOTA-G7N8 (MW ~ 20 kDa) was analyzed by radio-TLC on C18 plates, as described above.

PET Imaging. All PET images were acquired using a LabPET 8 scanner, while CT scans were performed on the preclinical MILabs U-CT scanner (b.v. Houten). A 60 min dynamic scan started immediately before the injection of 20 MBq (0.3 mL) of [^{64}Cu]Cu-NOTA-G7N8 via the tail vein. Static PET images were captured 30 min, 4 h, and 24 h postinjection. A subset of mice was coinjected with 100 mol equiv of unlabeled G7N8 (17 nmol). Throughout the scans, all animals' respiratory rate and temperature were monitored. PET images were reconstructed using the three-dimensional maximum likelihood expectation maximization (MLEM-3D) algorithm with 20 iterations and converted to percent injected dose per gram (% ID/g) based on a calibration phantom with a known activity concentration, assuming a tissue density of 1 g/cm³. Using PMOD software (version 3.8, PMOD Technology Ltd.), each mouse's PET image was coregistered with the corresponding CT image through rigid matching transformation. To quantify tumor uptake of the radiotracer, a volume of interest (VOI) was manually delineated on the CT image around the tumor and applied to the PET images. Uptake was calculated as the mean intensity of VOI voxels in the upper quartile. Additional VOIs were drawn for the kidneys, liver, and muscle. For the kidneys, an interactive thresholding method was employed to delineate the hot cortex on the PET image, while manual contours were drawn on CT slices for the liver and muscle. Uptake values for the kidneys, liver, and muscle were determined as the mean intensity of their respective VOI voxels.

Biodistribution. After the last PET scan, blood and organs mice were harvested. Blood was collected by femoral vein puncture using a heparin-coated syringe. The mice were then euthanized and dissected. Harvested tissues were rinsed, blotted dry, weighed, and their radioactivity was measured using a gamma counter (HIDEX AMG Gamma Counter 425–601). Results were reported as % ID/g.

Statistical Analysis. Data are presented as mean \pm (SD) and were analyzed using one-way ANOVA, two-way ANOVA, or two-tailed *t*-test in GraphPad Prism software. $P \leq 0.05$ was considered significant for all analyses.

■ ASSOCIATED CONTENT

Supporting Information

The Supporting Information is available free of charge at <https://pubs.acs.org/doi/10.1021/acs.jmedchem.5c00071>.

Additional experimental details on Nbs binding to GAL-7 in the presence of lactose, NMR studies, and the characterization of [^{64}Cu]Cu-NOTA-G7N8 are available in the Supporting Information PDF file (PDF)

GAL7-GAL7-G7N1-10models.pdb (PDB)

GAL7-GAL7-G7N2-10Models.pdb (PDB)

GAL7-GAL7-G7N3-10Models.pdb (PDB)

GAL7-GAL7-G7N4-10Models.pdb (PDB)

GAL7-GAL7-G7N5-10Models.pdb (PDB)

GAL7-GAL7-G7N6-10Models.pdb (PDB)

GAL7-GAL7-G7N7-10Models.pdb (PDB)

GAL7-GAL7-G7N8-10Models.pdb (PDB)

GAL7-GAL7-G7N9-10Models.pdb (PDB)

GAL7-GAL7-G7N10-10Models.pdb (PDB)

GAL7-GAL7-G7N11-10Models.pdb (PDB)

GAL7-GAL7-G7N12-10Models.pdb (PDB)

■ AUTHOR INFORMATION

Corresponding Author

Yves St-Pierre – INRS—Centre Armand-Frappier Santé Biotechnologie, Laval, Québec H7 V 1B7, Canada;

orcid.org/0000-0002-1948-2041; Phone: 450-687-5010;

Email: yves.st-pierre@inrs.ca; Fax: 450-686-5501

Authors

- Rita Nehmé – INRS—Centre Armand-Frappier Santé Biotechnologie, Laval, Québec H7 V 1B7, Canada
- Marlène Fortier – INRS—Centre Armand-Frappier Santé Biotechnologie, Laval, Québec H7 V 1B7, Canada
- Myriam Létourneau – INRS—Centre Armand-Frappier Santé Biotechnologie, Laval, Québec H7 V 1B7, Canada
- Camille Fuselier – INRS—Centre Armand-Frappier Santé Biotechnologie, Laval, Québec H7 V 1B7, Canada
- Philippine Granger Joly de Boissel – INRS—Centre Armand-Frappier Santé Biotechnologie, Laval, Québec H7 V 1B7, Canada
- Alyssa Dumoulin – INRS—Centre Armand-Frappier Santé Biotechnologie, Laval, Québec H7 V 1B7, Canada
- Brigitte Guérin – Department of Medical Imaging and Radiation Sciences, Faculty of Medicine and Health Sciences, Université de Sherbrooke, Sherbrooke, Québec J1H 5N4, Canada; orcid.org/0000-0002-0319-4512
- Véronique Dumulon-Perreault – Sherbrooke Molecular Imaging Center (CIMS)/Centre de Recherche du CHUS, Sherbrooke, Québec J1H 5N4, Canada
- Samia Ait-Mohand – Department of Medical Imaging and Radiation Sciences, Faculty of Medicine and Health Sciences, Université de Sherbrooke, Sherbrooke, Québec J1H 5N4, Canada
- Otman Sarrhini – Sherbrooke Molecular Imaging Center (CIMS)/Centre de Recherche du CHUS, Sherbrooke, Québec J1H 5N4, Canada
- Sacha T. Larda – INRS—Centre Armand-Frappier Santé Biotechnologie, Laval, Québec H7 V 1B7, Canada
- Yarileny Castellanos Villamizar – INRS—Centre Armand-Frappier Santé Biotechnologie, Laval, Québec H7 V 1B7, Canada
- Miguel Bernier – INRS—Centre Armand-Frappier Santé Biotechnologie, Laval, Québec H7 V 1B7, Canada
- Natalia Porębska – Department of Protein Engineering, Faculty of Biotechnology, University of Wrocław, Wrocław 50-383, Poland; orcid.org/0000-0002-1810-0232
- Lukasz Opaliński – Department of Protein Engineering, Faculty of Biotechnology, University of Wrocław, Wrocław 50-383, Poland; orcid.org/0000-0001-9656-8714
- David Chatenet – INRS—Centre Armand-Frappier Santé Biotechnologie, Laval, Québec H7 V 1B7, Canada
- Nicolas Doucet – INRS—Centre Armand-Frappier Santé Biotechnologie, Laval, Québec H7 V 1B7, Canada; orcid.org/0000-0002-1952-9380

Complete contact information is available at:

<https://pubs.acs.org/10.1021/acs.jmedchem.5c00071>

Author Contributions

The manuscript was conceived by R.N., M.F., M.L., B.G., L.O., DC. N.D., and Y.S.P. All authors were responsible for data interpretation and critical appraisal. All authors executed experiments and/or contributed to the experimental design and/or analyses. R.N. and Y.S.P. drafted the manuscript with input from all authors at all stages. All authors reviewed and approved the manuscript.

Funding

This work was supported by the Canadian Institutes of Health Research (CIHR), the Quantum Leap II program of the Consortium Québécois sur la Découverte du Médicament (CQDM), GlycoNet, and the Natural Sciences and Engineering

Research Council of Canada (NSERC) (Discovery grant RGPIN-2022-04368, to N.D.). Part of this work was also supported by the Molecular Interactions and Materials Characterization Facility (MIMC) of INRS, which is funded by a Canada Foundation for Innovation (CFI) Major Science Initiatives (MSI) fund awarded to GlycoNet Integrated Services. N.D. acknowledges support from a Research Scholar Senior Career Award (number 281993) of the Fonds de Recherche Québec—Santé (FRQS).

Notes

The authors declare the following competing financial interest(s): D.C., N.D., and Y.S.P. are co-inventors on multinational patent applications by Institut National de la Recherche Scientifique (INRS) related to this work, all dealing with the use of nanobodies and their use to inhibit a biological, physiological, and/or pathological process that involves GAL-7. All other authors report no conflicts.

ACKNOWLEDGMENTS

The authors acknowledge the support from scholarship and fellowship awards from the Arbour Foundation (R.N.), the Canadian Institutes of Health Research (CIHR) (R.N. and A.D.), and the Fonds de recherche du Québec - Nature et Technologies (FRQNT) (A.D.). The work of L.O. and N.P. was supported by SONATA BIS grant (2019/34/E/NZ3/00014) from the National Science Centre, Poland.

ABBREVIATIONS USED

ASF, asialofetuin; BLI, biolayer interferometry; CRD, carbohydrate recognition domain; GAL, galectin; GBS, glycan-binding sites; ipTM, interface predicted template modeling; Nbs, nanobodies; NOTA, 1,4,7-triazacyclononane-1,4,7-triacetic acid; PET, positron emission tomography; pTM, predicted template modeling; sdAb, single-domain antibody; TNBC, triple-negative breast cancer; % ID/g, percentage of injected dose per gram

REFERENCES

- (1) Cummings, R. D.; Liu, F. T.; Rabinovich, G. A.; Stowell, S. R.; Vasta, G. R. Galectins. In *Essentials of Glycobiology*, 4th ed.; Varki, A., Cummings, R. D., Esko, J. D., Stanley, P., Hart, G. W., Aebi, M., Mohnen, D., Kinoshita, T., Packer, N. H., Prestegard, J. H., Schaar, R. L., Seeberger, P. H., Eds.; Cold Spring Harbor Laboratory Press: Cold Spring Harbor, NY, 2022; Chapter 36.
- (2) Liu, F. T.; Rabinovich, G. A. Galectins as Modulators of Tumour Progression. *Nat. Rev. Cancer* **2005**, *5* (1), 29–41.
- (3) Gordon-Alonso, M.; Hirsch, T.; Wildmann, C.; van der Bruggen, P. Galectin-3 Captures Interferon- γ in the Tumor Matrix Reducing Chemokine Gradient Production and T-Cell Tumor Infiltration. *Nat. Commun.* **2017**, *8* (1), 793.
- (4) Girotti, M. R.; Salatino, M.; Dalotto-Moreno, T.; Rabinovich, G. A. Sweetening the Hallmarks of Cancer: Galectins as Multifunctional Mediators of Tumor Progression. *J. Exp. Med.* **2020**, *217* (2), No. e20182041.
- (5) Sanjurjo, L.; Broekhuizen, E. C.; Koenen, R. R.; Thijssen, V. L. J. L. Galectokines: The Promiscuous Relationship between Galectins and Cytokines. *Biomolecules* **2022**, *12* (9), 1286.
- (6) Mariño, K. V.; Cagnoni, A. J.; Croci, D. O.; Rabinovich, G. A. Targeting Galectin-Driven Regulatory Circuits in Cancer and Fibrosis. *Nat. Rev. Drug Discovery* **2023**, *22* (4), 295–316.
- (7) Perillo, N. L.; Pace, K. E.; Seilhamer, J. J.; Baum, L. G. Apoptosis of T Cells Mediated by Galectin-1. *Nature* **1995**, *378* (6558), 736–739.
- (8) Hahn, H. P.; Pang, M.; He, J.; Hernandez, J. D.; Yang, R. Y.; Li, L. Y.; Wang, X.; Liu, F. T.; Baum, L. G. Galectin-1 Induces Nuclear Translocation of Endonuclease G in Caspase- and Cytochrome c-

- Independent T Cell Death. *Cell Death Differ.* **2004**, *11* (12), 1277–1286.
- (9) Derosiers, N.; Aguilar, W.; DeGaramo, D. A.; Posey, A. D. Sweet Immune Checkpoint Targets to Enhance T Cell Therapy. *J. Immunol.* **2022**, *208* (2), 278–285.
- (10) Kapetanakis, N. I.; Busson, P. Galectins as Pivotal Components in Oncogenesis and Immune Exclusion in Human Malignancies. *Front. Immunol.* **2023**, *14*, 1145268.
- (11) Magnaldo, T.; Fowles, D.; Darmon, M. Galectin-7, a Marker of All Types of Stratified Epithelia. *Differentiation* **1998**, *63* (3), 159–168.
- (12) Sato, M.; Nishi, N.; Shoji, H.; Kumagai, M.; Imaizumi, T.; Hata, Y.; Hirashima, M.; Suzuki, S.; Nakamura, T. Quantification of Galectin-7 and Its Localization in Adult Mouse Tissues. *J. Biochem.* **2002**, *131* (2), 255–260.
- (13) Advedissian, T.; Deshayes, F.; Viguier, M. Galectin-7 in Epithelial Homeostasis and Carcinomas. *Int. J. Mol. Sci.* **2017**, *18* (12), 2760.
- (14) Cao, Z.; Said, N.; Amin, S.; Wu, H. K.; Bruce, A.; Garate, M.; Hsu, D. K.; Kuwabara, I.; Liu, F. T.; Panjwani, N. Galectins-3 and -7, but Not Galectin-1, Play a Role in Re-Epithelialization of Wounds. *J. Biol. Chem.* **2002**, *277* (44), 42299–42305.
- (15) Cao, Z.; Said, N.; Wu, H. K.; Kuwabara, I.; Liu, F. T.; Panjwani, N. Galectin-7 as a Potential Mediator of Corneal Epithelial Cell Migration. *Arch. Ophthalmol.* **2003**, *121* (1), 82–86.
- (16) Menkhorst, E.; Zhou, W.; Santos, L. L.; Delforce, S.; So, T.; Rainczuk, K.; Loke, H.; Syngelaki, A.; Varshney, S.; Williamson, N.; Pringle, K.; Young, M. J.; Nicolaidis, K. H.; St-Pierre, Y.; Dimitriadis, E. Galectin-7 Impairs Placentation and Causes Preeclampsia Features in Mice. *Hypertension* **2020**, *76* (4), 1185–1194.
- (17) Lu, J.; Pei, H.; Kaeck, M.; Thompson, H. J. Gene Expression Changes Associated with Chemically Induced Rat Mammary Carcinogenesis. *Mol. Carcinog.* **1997**, *20* (2), 204–215.
- (18) Demers, M.; Magnaldo, T.; St-Pierre, Y. A Novel Function for Galectin-7: Promoting Tumorigenesis by Up-Regulating MMP-9 Gene Expression. *Cancer Res.* **2005**, *65* (12), 5205–5210.
- (19) St-Pierre, Y.; Campion, C. G.; Grosset, A. A. A Distinctive Role for Galectin-7 in Cancer? *Front. Biosci. (Landmark Ed.)* **2012**, *17* (2), 438–450.
- (20) Demers, M.; Rose, A. A.; Grosset, A. A.; Biron-Pain, K.; Gaboury, L.; Siegel, P. M.; St-Pierre, Y. Overexpression of Galectin-7, a Myoepithelial Cell Marker, Enhances Spontaneous Metastasis of Breast Cancer Cells. *Am. J. Pathol.* **2010**, *176* (6), 3023–3031.
- (21) Wu, G.; Deng, W.; Chen, H. Y.; Cho, H. J.; Kim, J. Galectin-7 Leads to a Relative Reduction in CD4+ T Cells, Mediated by PD-1. *Sci. Rep.* **2024**, *14* (1), 6625.
- (22) An, J.; Nagaki, Y.; Motoyama, S.; Kuze, Y.; Hoshizaki, M.; Kemuriyama, K.; Yamaguchi, T.; Ebihara, T.; Minamiya, Y.; Suzuki, Y.; Imai, Y.; et al. Identification of Galectin-7 as a Crucial Metastatic Enhancer of Squamous Cell Carcinoma Associated with Immunosuppression. *Oncogene* **2022**, *41* (50), 5319–5330.
- (23) Laderach, D. J.; Compagno, D. Inhibition of Galectins in Cancer: Biological Challenges for Their Clinical Application. *Front. Immunol.* **2023**, *13*, 1104625.
- (24) Vladoiu, M. C.; Labrie, M.; St-Pierre, Y. Intracellular Galectins in Cancer Cells: Potential New Targets for Therapy. *Int. J. Oncol.* **2014**, *44* (4), 1001–1014.
- (25) Moutel, S.; Bery, N.; Bernard, V.; Keller, L.; Lemesre, E.; de Marco, A.; Ligat, L.; Rain, J. C.; Favre, G.; Olichon, A.; Perez, F. NaLi-H1: A Universal Synthetic Library of Humanized Nanobodies Providing Highly Functional Antibodies and Intrabodies. *Elife* **2016**, *5*, No. e16228.
- (26) Saussez, S.; Decaestecker, C.; Lorfèvre, F.; Chevalier, D.; Mortuaire, G.; Kaltner, H.; André, S.; Toubeau, G.; Gabius, H. J.; Leroy, X. Increased Expression and Altered Intracellular Distribution of Adhesion/Growth-Regulatory Lectins Galectins-1 and -7 During Tumour Progression in Hypopharyngeal and Laryngeal Squamous Cell Carcinomas. *Histopathology* **2008**, *52* (4), 483–493.
- (27) Labrie, M.; De Araujo, L. O. F.; Communal, L.; Mes-Masson, A. M.; St-Pierre, Y. Tissue and Plasma Levels of Galectins in Patients with High-Grade Serous Ovarian Carcinoma as New Predictive Biomarkers. *Sci. Rep.* **2017**, *7* (1), 13244.
- (28) Schulz, H.; Schmoedel, E.; Kuhn, C.; Hofmann, S.; Mayr, D.; Mahner, S.; Jeschke, U. Galectins-1, -3, and -7 Are Prognostic Markers for Survival of Ovarian Cancer Patients. *Int. J. Mol. Sci.* **2017**, *18* (6), 1230.
- (29) Brito, L. N. S.; de Lemos Almeida, M. M. R.; de Souza, L. B.; Alves, P. M.; Nonaka, C. F. W.; Godoy, G. P. Immunohistochemical Analysis of Galectins-1, -3, and -7 in Periapical Granulomas, Radicular Cysts, and Residual Radicular Cysts. *J. Endod.* **2018**, *44* (5), 728–733.
- (30) Vladoiu, M. C.; Labrie, M.; Létourneau, M.; Egesborg, P.; Gagné, D.; Billard, E.; Grosset, A. A.; Doucet, N.; Chatenet, D.; St-Pierre, Y. Design of a Peptidic Inhibitor That Targets the Dimer Interface of a Prototypic Galectin. *Oncotarget* **2015**, *6* (38), 40970–40980.
- (31) Walzel, H.; Blach, M.; Hirabayashi, J.; Kasai, K. I.; Brock, J. Involvement of CD2 and CD3 in Galectin-1 Induced Signaling in Human Jurkat T-Cells. *Glycobiology* **2000**, *10* (2), 131–140.
- (32) Brandt, B.; Büchse, T.; Abou-Eladab, E. F.; Tiedge, M.; Krause, E.; Jeschke, U.; Walzel, H. Galectin-1 Induced Activation of the Apoptotic Death-Receptor Pathway in Human Jurkat T Lymphocytes. *Histochem. Cell Biol.* **2008**, *129* (5), 599–609.
- (33) Norambuena, A.; Metz, C.; Vicuña, L.; Silva, A.; Pardo, E.; Oyanadel, C.; Massardo, L.; González, A.; Soza, A. Galectin-8 Induces Apoptosis in Jurkat T Cells by Phosphatidic Acid-Mediated ERK1/2 Activation Supported by Protein Kinase A Down-Regulation. *J. Biol. Chem.* **2009**, *284* (19), 12670–12679.
- (34) Abramson, J.; Adler, J.; Dunger, J.; Evans, R.; Green, T.; Pritzel, A.; Ronneberger, O.; Willmore, L.; Ballard, A. J.; Bambrick, J.; Bodenstein, S. W.; Evans, D. A.; Hung, C. C.; O'Neill, M.; Reiman, D.; Tunyasuvunakool, K.; Wu, Z.; Zemgulyte, A.; Arvaniti, E.; Beattie, C.; Bertolli, O.; Bridgland, A.; Cherepanov, A.; Congreve, M.; Cowen-Rivers, A. I.; Cowie, A.; Figurnov, M.; Fuchs, F. B.; Gladman, H.; Jain, R.; Khan, Y. A.; Low, C. M. R.; Perlin, K.; Potapenko, A.; Savy, P.; Singh, S.; Stecula, A.; Thillaisundaram, A.; Tong, C.; Yakneen, S.; Zhong, E. D.; Zielinski, M.; Židek, A.; Bapst, V.; Kohli, P.; Jaderberg, M.; Hassabis, D.; Jumper, J. M. Accurate Structure Prediction of Biomolecular Interactions with AlphaFold 3. *Nature* **2024**, *630* (8016), 493–500.
- (35) Muyldermans, S. Nanobodies Natural Single-Domain Antibodies. *Annu. Rev. Biochem.* **2013**, *82*, 775–797.
- (36) Zhang, Y.; Skolnick, J. Scoring Function for Automated Assessment of Protein Structure Template Quality [Published Correction Appears in Proteins, 2007, 68 (4), 1020]. *Proteins* **2004**, *57* (4), 702–710.
- (37) Xu, J.; Zhang, Y. How Significant Is a Protein Structure Similarity with TM-Score = 0.5? *Bioinformatics* **2010**, *26* (7), 889–895.
- (38) Pham, N. T. H.; Létourneau, M.; Fortier, M.; Bégin, G.; Al-Abdul-Wahid, M. S.; Pucci, F.; Folch, B.; Rومان, M.; Chatenet, D.; St-Pierre, Y.; Lagüe, P.; Calmettes, C.; Doucet, N. Perturbing Dimer Interactions and Allosteric Communication Modulates the Immunosuppressive Activity of Human Galectin-7. *J. Biol. Chem.* **2021**, *297* (5), 101308.
- (39) Ermakova, E.; Miller, M. C.; Nesmelova, I. V.; López-Merino, L.; Berbis, M. A.; Nesmelov, Y.; Tkachev, Y. V.; Lagartera, L.; Daragan, V. A.; André, S.; Cañada, F. J.; Jiménez-Barbero, J.; Solís, D.; Gabius, H. J.; Mayo, K. H. Lactose Binding to Human Galectin-7 (p53-Induced Gene 1) Induces Long-Range Effects Through the Protein Resulting in Increased Dimer Stability and Evidence for Positive Cooperativity. *Glycobiology* **2013**, *23* (5), 508–523.
- (40) Ewens, A.; Mihich, E.; Ehrke, M. J. Distant Metastasis from Subcutaneously Grown E0771 Medullary Breast Adenocarcinoma. *Anticancer Res.* **2005**, *25* (6B), 3905–3915.
- (41) Yang, E. Y.; Shah, K. Nanobodies: Next Generation of Cancer Diagnostics and Therapeutics. *Front. Oncol.* **2020**, *10*, 1182.
- (42) Takata, T.; Ishigaki, Y.; Shimasaki, T.; Tsuchida, H.; Motoo, Y.; Hayashi, A.; Tomosugi, N. Characterization of Proteins Secreted by Pancreatic Cancer Cells with Anticancer Drug Treatment In Vitro. *Oncol. Rep.* **2012**, *28* (6), 1968–1976.

- (43) Dubé-Delarosbil, C.; St-Pierre, Y. The Emerging Role of Galectins in High-Fatality Cancers. *Cell. Mol. Life Sci.* **2018**, *75* (7), 1215–1226.
- (44) Sewgobind, N. V.; Albers, S.; Pieters, R. J. Functions and Inhibition of Galectin-7, an Emerging Target in Cellular Pathophysiology. *Biomolecules* **2021**, *11* (11), 1720.
- (45) Bansal, A.; Lavoie, R. R.; Lucien, F.; Kethamreddy, M.; Wootla, B.; Dong, H.; Park, S. S.; Pandey, M. K. Synthesis and Evaluation of Anti-PD-L1-B11 Antibody Fragments for PET Imaging of PD-L1 in Breast Cancer and Melanoma Tumor Models. *Sci. Rep.* **2024**, *14* (1), 19561.
- (46) Zhang, Y.; Cao, M.; Wu, Y.; Malih, S.; Xu, D.; Yang, E.; Younis, M. H.; Lin, W.; Zhao, H.; Wang, C.; Liu, Q.; et al. Preclinical Development of Novel PD-L1 Tracers and First-in-Human Study of [⁶⁸Ga]Ga-NOTA-RW102 in Patients with Lung Cancers. *J. Immunother. Cancer* **2024**, *12* (4), No. e008794.
- (47) Zhao, L.; Gong, J.; Liao, S.; Huang, W.; Zhao, J.; Xing, Y. Preclinical Evaluation and Preliminary Clinical Study of ⁶⁸Ga-NODAGA-NM-01 for PET Imaging of PD-L1 Expression. *Cancer Imaging* **2025**, *25* (1), 6.
- (48) Ingram, J. R.; Schmidt, F. I.; Ploegh, H. L. Exploiting Nanobodies' Singular Traits. *Annu. Rev. Immunol.* **2018**, *36*, 695–715.
- (49) Li, B.; Qin, X.; Mi, L. Z. Nanobodies From Structure to Applications in Non-Injectable and Bispecific Biotherapeutic Development. *Nanoscale* **2022**, *14* (19), 7110–7122.
- (50) Xie, Y. J.; Dougan, M.; Jaikhani, N.; Ingram, J.; Fang, T.; Kummer, L.; Momin, N.; Pishesha, N.; Rickelt, S.; Hynes, R. O.; Ploegh, H. Nanobody-Based CAR T Cells That Target the Tumor Microenvironment Inhibit the Growth of Solid Tumors in Immunocompetent Mice. *Proc. Natl. Acad. Sci. U.S.A.* **2019**, *116* (16), 7624–7631.
- (51) Singh, R. K.; Soliman, A.; Guitoli, G.; Störmer, E.; von Zweydford, F.; Dal Maso, T.; Oun, A.; Van Rillaer, L.; Schmidt, S. H.; Chatterjee, D.; David, J. A.; Pardon, E.; Schwartz, T. U.; Knapp, S.; Kennedy, E. J.; Steyaert, J.; Herberg, F. W.; Kortholt, A.; Gloeckner, C. J.; Versées, W. Nanobodies as Allosteric Modulators of Parkinson's Disease-Associated LRRK2. *Proc. Natl. Acad. Sci. U.S.A.* **2022**, *119* (9), No. e2112712119.
- (52) Gauthier, L.; Rossi, B.; Roux, F.; Termine, E.; Schiff, C. Galectin-1 Is a Stromal Cell Ligand of the Pre-B Cell Receptor (BCR) Implicated in Synapse Formation between Pre-B and Stromal Cells and in Pre-BCR Triggering. *Proc. Natl. Acad. Sci. U.S.A.* **2002**, *99* (20), 13014–13019.
- (53) Shimura, T.; Takenaka, Y.; Tsutsumi, S.; Hogan, V.; Kikuchi, A.; Raz, A. Galectin-3, a Novel Binding Partner of β -Catenin. *Cancer Res.* **2004**, *64* (18), 6363–6367.
- (54) Satelli, A.; Rao, P. S.; Thirumala, S.; Rao, U. S. Galectin-4 Functions as a Tumor Suppressor of Human Colorectal Cancer. *Int. J. Cancer* **2011**, *129* (4), 799–809.
- (55) Villeneuve, C.; Baricault, L.; Canelle, L.; Barboule, N.; Racca, C.; Monsarrat, B.; Magnaldo, T.; Larminat, F. Mitochondrial Proteomic Approach Reveals Galectin-7 as a Novel BCL-2 Binding Protein in Human Cells. *Mol. Biol. Cell* **2011**, *22* (7), 999–1013.
- (56) Labrie, M.; Vladoiu, M.; Leclerc, B. G.; Grosset, A. A.; Gaboury, L.; Stagg, J.; St-Pierre, Y. A Mutation in the Carbohydrate Recognition Domain Drives a Phenotypic Switch in the Role of Galectin-7 in Prostate Cancer. *PLoS One* **2015**, *10* (7), No. e0131307.
- (57) Fuselier, C.; Dumoulin, A.; Paré, A.; Nehmé, R.; Ajarrag, S.; Granger Joly de Boissel, P.; Chatenet, D.; Doucet, N.; St-Pierre, Y. Placental Galectins in Cancer: Why We Should Pay More Attention. *Cells* **2023**, *12* (3), 437.
- (58) Vranken, W. F.; Boucher, W.; Stevens, T. J.; Fogh, R. H.; Pajon, A.; Llinas, M.; Ulrich, E. L.; Markley, J. L.; Ionides, J.; Laue, E. D. The CCPN Data Model for NMR Spectroscopy: Development of a Software Pipeline. *Proteins* **2005**, *59* (4), 687–696.
- (59) Stark, J.; Powers, R. Rapid Protein-Ligand Costructures Using Chemical Shift Perturbations. *J. Am. Chem. Soc.* **2008**, *130* (2), 535–545.
- (60) Williamson, M. P. Using Chemical Shift Perturbation to Characterize Ligand Binding [Published Correction Appears in *Prog. Nucl. Magn. Reson. Spectrosc.* 2014, 80, 64]. *Prog. Nucl. Magn. Reson. Spectrosc.* **2013**, *73*, 1–16.
- (61) Walker, J. M. The Bicinchoninic Acid (BCA) Assay for Protein Quantitation. *Methods Mol. Biol.* **1994**, *32*, 5–8.
- (62) Meares, C. F.; McCall, M. J.; Reardan, D. T.; Goodwin, D. A.; Diamanti, C. I.; McTigue, M. Conjugation of Antibodies with Bifunctional Chelating Agents: Isothiocyanate and Bromoacetamide Reagents, Methods of Analysis, and Subsequent Addition of Metal Ions. *Anal. Biochem.* **1984**, *142* (1), 68–78.